INTERNATIONAL JOURNAL FOR NUMERICAL METHODS IN FLUIDS
*Int. J. Numer. Meth. Fluids* 2016; **00**:1–**??**
Published online in Wiley Online Library (www.onlinelibrary.wiley.com). DOI: 10.1002/fld.4262

Accepted Article

# An improved ghost-cell immersed boundary method for compressible flow simulations

Cheng Chi, Bok Jik Lee*and Hong G. Im

*Clean Combustion Research Center, King Abdullah University of Science and Technology (KAUST), Thuwal 23955-6900, Saudi Arabia*

SUMMARY

This study presents an improved ghost-cell immersed boundary approach to represent a solid body in compressible flow simulations. In contrast to the commonly used approaches, in the present work ghost cells are mirrored through the boundary described using a level-set method to farther image points, incorporating a higher-order extra/interpolation scheme for the ghost cell values. A sensor is introduced to deal with image points near the discontinuities in the flow field. Adaptive mesh refinement (AMR) is used to improve the representation of the geometry efficiently in the Cartesian grid system. The improved ghost-cell method is validated against four test cases: (a) double Mach reflections on a ramp, (b) smooth Prandtl-Meyer expansion flows, (c) supersonic flows in a wind tunnel with a forward-facing step, and (d) supersonic flows over a circular cylinder. It is demonstrated that the improved ghost-cell method can reach the accuracy of second order in $L^1$ norm and higher than first order in $L^\infty$ norm. Direct comparisons against the cut-cell method demonstrate that the improved ghost-cell method is almost equally accurate with better efficiency for boundary representation in high-fidelity compressible flow simulations. Copyright © 2016 John Wiley & Sons, Ltd.

Received . . .

KEY WORDS: compressible flow; Cartesian grid; immersed boundary; ghost-cell method; level-set method; cut-cell method

*Correspondence to: E-mail: bokjik.lee@kaust.edu.sa

This article has been accepted for publication and undergone full peer review but has not been through the copyediting, typesetting, pagination and proofreading process, which may lead to differences between this version and the Version of Record. Please cite this article as doi: 10.1002/fld.4262

This article is protected by copyright. All rights reserved.

## 1. INTRODUCTION

With the advances in the computing power, high fidelity computational fluid dynamics (CFD) simulations increasingly employ complex geometries within the computational domain. While a non-Cartesian body-fitted grid system is advantageous for dealing with general geometry of solid boundaries, the Cartesian grid system, in favor of its simplicity and regularity in grid structure, remains a preferred choice especially in applications that can benefit from adaptive mesh refinement (AMR).

To avoid the inferior accuracy associated with a stair-case-like representation, two approaches to capture the solid boundaries are commonly adopted: cut-cell and ghost-cell methods. In cut-cell methods [1–4], near-boundary computational cells are cut by the true physical boundary and the fluxes on the cut surface are computed by elaborate interpolation schemes. Although the cut-cell method has an advantage of ensuring conservation of mass and momentum at the boundary, cell reshaping may generate extremely small cells, thereby limiting the time-step due to the required stability conditions and thus resulting in a steep increase in the computational cost. Some remedies to the small-cell problems have been proposed, such as cell-merging technique [1, 5], rotating box method [3], and flux-redistribution procedure [2, 6–10]. Nevertheless, the cut-cell approach in general requires complex algorithms in implementation.

Alternatively, in ghost-cell methods [11], cells neighboring the solid boundary are identified as ghost cells, which implicitly incorporate conditions to be satisfied at the boundary. Ghost-cell methods are often coupled with a level-set method [12] to deal with complex geometry or interfaces. The detailed ghost-cell/level-set implementation can be found in [13–16]. In general, ghost-cell methods are considered to be less accurate than the cut-cell method at the same resolution of the base Cartesian grid due to its inherent implicit representation of the solid boundary. Nevertheless, ghost-cell methods are advantageous in favor of the easy implementation and computational efficiency as it is not necessary to modify flux calculations of existing Cartesian-system based codes, and the complicated cell reshaping procedure is not needed. The accuracy of ghost-cell methods is determined by how the ghost-cell variables are extra/interpolated through the boundary. A classical scheme computing ghost-cell values is the bilinear interpolation (trilinear for three-dimensional cases) for symmetrically mirrored points. However, when the mirrored point is too close to the boundary, it may encounter a difficult situation that, for example in a 2D case, four surrounding points required for the bilinear interpolation are not all in the fluid domain. If such a "too-close ghost-cell" issue [17] happens, the missing points can be reconstructed by a zeroth-order extrapolation [18] or using body-intercepting points for interpolation [19, 20]. However, the former approach may result in a sole zeroth-order extrapolation if there is only one point is left for the interpolation, and the latter approach becomes difficult to implement for Neumann-type boundary conditions.

Therefore, the main objective of the study is to propose and implement a modified ghost-cell/level-set method with improved accuracy without additional complexities in the implementation. The proposed method deals with the too-close ghost-cell issue by reconstructing the value at ghost cells that are too close to the boundary by utilizing farther points inside the fluid domain, thereby achieving complete bilinear interpolations at image points. The idea was first proposed for incompressible flow simulations [21], but has not been demonstrated in compressible flow simulations. To estimate the robustness and accuracy of the proposed ghost-cell method, simulation results over a range of selected test problems are presented and discussed in comparison to those from a ghost-cell method using zeroth order extrapolation [18] for too-close ghost cells, and to those from a cut-cell method available from the Chombo package [22, 23].

The paper is organized as follows. In section 2, the system of equations considered in the present study and numerical methods are described in detail. In the following section 3, numerical simulation results are presented and discussed for a number of selected test cases: double Mach reflection, Prandtl-Meyer expansion, forward-facing step, and supersonic flow over a circular cylinder. Summary and concluding remarks are presented in section 4.

This article is protected by copyright. All rights reserved.

Accepted Article

## 2. FORMULATION AND NUMERICAL METHOD

### 2.1. Governing equations

As a first development for compressible flow solvers, inviscid Euler equations are chosen for the demonstration of the capability of the proposed ghost-cell method. Extension to viscous Navier-Stokes equations is straightforward and will be conducted in future studies. The conservation equations for mass, momentum, and energy equations are written as:

$$\frac{\partial \rho}{\partial t} + \nabla \cdot (\rho \mathbf{u}) = 0 \tag{1}$$

$$\frac{\partial (\rho \mathbf{u})}{\partial t} + \nabla \cdot (\rho \mathbf{u}\mathbf{u}) + \nabla p = 0 \tag{2}$$

$$\frac{\partial E}{\partial t} + \nabla \cdot ((E+p)\mathbf{u}) = 0 \tag{3}$$

where $\rho, \mathbf{u}, p, E$ denote the density, velocity, pressure, and total specific energy, respectively. With the ideal gas equation of states, total specific energy $E$ and speed of sound $c$ are written as

$$E = \frac{p}{\gamma - 1} + \frac{1}{2}\rho \mathbf{u}^2, \quad c = \sqrt{\frac{\gamma p}{\rho}}. \tag{4}$$

### 2.2. The Godunov method

Equations (1), (2) and (3) are written in conservative form for two-dimensional space as follows:

$$\mathbf{U}_t + \mathbf{F}(\mathbf{U})_x + \mathbf{G}(\mathbf{U})_y = 0 \tag{5}$$

with

$$\mathbf{U} = \begin{bmatrix} \rho \\ \rho u \\ \rho v \\ E \end{bmatrix}, \mathbf{F}(\mathbf{U}) = \begin{bmatrix} \rho u \\ \rho u^2 + p \\ \rho uv \\ u(E+p) \end{bmatrix}, \mathbf{G}(\mathbf{U}) = \begin{bmatrix} \rho v \\ \rho uv \\ \rho v^2 + p \\ v(E+p) \end{bmatrix} \tag{6}$$

Using a finite volume method, within each cell $I_{i,j} = [x_{i-\frac{1}{2}}, x_{i+\frac{1}{2}}; y_{j-\frac{1}{2}}, y_{j+\frac{1}{2}}]$, equation (5) is discretized in space and time as

$$\mathbf{U}_{i,j}^{n+1} = \mathbf{U}_{i,j}^{n} + \frac{\Delta t}{\Delta x}[\mathbf{F}_{i-\frac{1}{2}}^{n+1/2} - \mathbf{F}_{i+\frac{1}{2}}^{n+1/2}] + \frac{\Delta t}{\Delta y}[\mathbf{G}_{j-\frac{1}{2}}^{n+1/2} - \mathbf{G}_{j+\frac{1}{2}}^{n+1/2}] \tag{7}$$

with numerical fluxes at cell interfaces given by

$$\mathbf{F}_{i+\frac{1}{2}}^{n+1/2} = \mathbf{F}(\mathbf{U}_{i+\frac{1}{2}}^{n+1/2}), \ \mathbf{G}_{j+\frac{1}{2}}^{n+1/2} = \mathbf{G}(\mathbf{U}_{j+\frac{1}{2}}^{n+1/2}) \tag{8}$$

The piecewise parabolic method (PPM) introduced by Colella and Woodward [24] is adopted for the approximation of time-centered edge states $\mathbf{U}_{j+\frac{1}{2}}^{n+1/2}$. In the PPM algorithm, the left and right state of primitive variables $\mathbf{Q}(\rho, u, v, p)$ at each cell edge are extrapolated from the base-time data in space and time, using the characteristic wave propagation formulas. The reconstruction for the variables in each cell is parabolic. The cell edge state is further limited by the van Leer slope limiter. After the left state $\mathbf{Q}_L(\rho_L, u_L, v_L, p_L)$ and the right state $\mathbf{Q}_R(\rho_R, u_R, v_R, p_R)$ of the cell edge are reconstructed, a Riemann problem is established for each cell edge. The cell edge numerical fluxes $\mathbf{F}^{n+1/2}$ and $\mathbf{G}^{n+1/2}$ can be constructed using a Riemann solver.

This article is protected by copyright. All rights reserved.

Accepted Article

### 2.3. The Riemann solver

The Riemann solver used for this study is the primitive variable Riemann solver (PVRS) [25], an approximate Riemann solver with which the starred values are obtained as following:

$$p^* = \frac{C_L p_R + C_R p_L + C_L C_R (u_L - u_R)}{C_L + C_R}, \tag{9}$$

$$u^* = \frac{C_L u_L + C_R u_R + (p_L - p_R)}{C_L + C_R}, \tag{10}$$

$$v^*_{L,R} = v_{L,R}, \text{ and} \tag{11}$$

$$\rho^*_{L,R} = \rho_{L,R} + \frac{p^* - p_{L,R}}{(a^*_{L,R})^2}, \tag{12}$$

where

$$(a^*_{L,R})^2 = \gamma p^* / \rho^*_{L,R} \text{ and} \tag{13}$$

$$C_{L,R} = \sqrt{\gamma p_{L,R} \rho_{L,R}}. \tag{14}$$

In the above, $v$ refers to advected quantities including transverse velocity components, $_{L,R}$ represents the left and right states for the Riemann problem and $^*_{L,R}$ represents values on the left and right side of the contact discontinuity.

After the starred variables are determined, the solution is sampled to find the interface value of the primitive variables, $\mathbf{Q}^{n+1/2}(0)$, which are finally converted to the conservative variables, $\mathbf{U}^{n+1/2}(0)$. Subsequently, the Godunov fluxes $\mathbf{F}^{n+1/2}$ and $\mathbf{G}^{n+1/2}$ can be computed by equation (8).

### 2.4. Ghost-cell immersed boundary method

A ghost-cell method is adopted to implement boundary conditions for the immersed boundaries without modifying the overall finite-volume algorithms. In the present ghost-cell method, the boundary conditions are incorporated implicitly by defining ghost-cell values appropriately. For the Euler equations under study, slip-wall boundary conditions along the immersed geometries are developed.

#### 2.4.1. Adaptive mesh refinement

Representation of immersed boundaries in the Cartesian grid system can be improved using adaptive mesh refinement (AMR) which can be applied not only to regions of large gradient in the fluid domain but also to the boundaries of geometry. A block-structured AMR method based on the BoxLib [26] is adopted in the present study. The BoxLib framework supports all the functionality needed to write a parallel AMR application. For the present hyperbolic system, the refinement of the nested grid hierarchy is simultaneous in both time and space.

#### 2.4.2. The level-set method

To accurately represent the solid wall boundary intersecting with the Cartesian grid, the necessary geometric information needs to be stored for the ghost cell projection process. For this purpose, the level-set method introduced by Osher and Sethian [27] is adopted. Further details on the subsequent development and refinements of the level-set method can be found in [12, 28, 29].

Two-dimensional, stationary level-set cases are considered in the present study. A level-set function $\phi(x, y)$ is defined using a signed distance from point $(x, y)$ to the immersed boundary. The absolute distance to the interface $|\phi(x, y)|$ and the normal vector $\nabla\phi(x, y)$ of the isoline of $\phi$ are utilized to determine the relative positions of the image points of ghost cells and to compute the extrapolated ghost cell values.

This article is protected by copyright. All rights reserved.

Accepted Article

*2.4.3. The baseline ghost-cell method*

The conventional bilinear interpolation scheme available in the AMROC package [18] is referred to as the baseline ghost-cell method in the subsequent discussion. As illustrated in Fig. 1, an image point of a ghost cell is symmetrically mirrored through the boundary such that

$$\mathbf{r}_{image} = -\mathbf{r}_{ghost} \tag{15}$$

where $\mathbf{r}_{image}$ is the distance vector from the projection point to the image point and $\mathbf{r}_{ghost}$ is the distance vector from the projection point to the ghost point, i.e. the center of the ghost cell. The state values at the image point are then defined using a bilinear interpolation from surrounding cell-centered values available. The baseline ghost-cell method finds the values at the image points using a complete bilinear interpolation when available, or using an incomplete bilinear interpolation when the ghost cell is too close to the boundary. If there are missing points to construct bilinear interpolation, they are extrapolated from either the horizontal neighboring point or the vertical neighboring point depending on the sequential order of the interpolation.

Once the location and values of the image points of the ghost cells are identified, the boundary conditions for the projection points are applied to construct the ghost cell values as

$$\mathbf{q}|_{ghost} = \mathbf{q}|_{image}, \text{ and} \tag{16}$$

$$u_n|_{ghost} = -u_n|_{image}, \tag{17}$$

where $u_n$ is the velocity component normal to the boundary and $\mathbf{q}$ contains all other primitive variables including $u_t$, the velocity component tangential to the boundary.

The baseline ghost-cell method is straightforward in implementation and is known to be computationally stable. A critical problem, however, arises when the incomplete bilinear interpolation is applied to the ghost cells closer to the boundary, resulting in degradation of numerical accuracy. An improvement is suggested in the present study as follows.

*2.4.4. Improved ghost-cell method*

An improved ghost-cell method is proposed, in order to ensure complete bilinear interpolations in the construction of image point values. This concept has been introduced in [21] for incompressible flows, and is extended to compressible flows in this study. In this method, when the distance between ghost-cell node and the immersed boundary is smaller than a specified threshold, the image point is projected to a farther distance in the fluid domain as illustrated in Fig. 2. The distance $\delta$ must be large enough to ensure the image point to be completely enclosed by a set of four neighboring fluid cells; however, an excessive large distance $\delta$ may result in incorrect physical description of the boundary condition. It is thus suggested that a threshold distance is defined as $\delta = \sqrt{2}\Delta x$ in two-dimensional cases, where $\Delta x$ is the cell size. Furthermore, for a quadratic extrapolation for the boundary conditions, an extra image point is defined by a distance vector, $\mathbf{r}_{extra}$, from the image point to the extra image point.

For the Euler equations under study, slip-wall boundary conditions are considered:

$$u_n|_{proj} = 0 \tag{18}$$

$$\frac{\partial \mathbf{q}}{\partial n}|_{proj} = 0 \tag{19}$$

where $n$ is the coordinate normal to the wall boundary, $u_n$ is the velocity component normal to the boundary, and $\mathbf{q}$ represents all other primitive variables including $u_t$. Note that (18) is a Dirichlet and (19) is a Neumann boundary condition. While the formulations are presented based on these specific boundary conditions, the method is generally applicable to any other general boundary conditions encountered in the Navier-Stokes equations.

The main goal is to derive equations to determine the ghost-cell values for $\mathbf{q}$ and $u_n$, using (19) and (18), respectively. First, to determine the expression for $\mathbf{q}$, it is assumed that the normal gradients of the solution vector, $\frac{\partial \mathbf{q}}{\partial n}$, at the ghost cell, at the projection point, and at the image point are linearly related along the normal distance from the boundary, yielding

This article is protected by copyright. All rights reserved.

$$\frac{\partial \mathbf{q}}{\partial n}|_{ghost} = \frac{\partial \mathbf{q}}{\partial n}|_{proj} - |\mathbf{r}_{ghost}| \cdot s_0 \tag{20}$$

where $s_0$ is the slope defined by

$$s_0 = \frac{\frac{\partial \mathbf{q}}{\partial n}|_{image} - \frac{\partial \mathbf{q}}{\partial n}|_{proj}}{\delta}. \tag{21}$$

Applying the boundary condition (19), equation (20) is written as

$$\begin{aligned} \frac{\partial \mathbf{q}}{\partial n}|_{ghost} &= 0 - |\mathbf{r}_{ghost}| \cdot \frac{\frac{\partial \mathbf{q}}{\partial n}|_{image} - 0}{\delta} \\ &= -|\mathbf{r}_{ghost}| \cdot \frac{\frac{\partial \mathbf{q}}{\partial n}|_{image}}{\delta}. \end{aligned} \tag{22}$$

It is still difficult to directly compute $\mathbf{q}|_{ghost}$ from (22). Therefore, the mirrored point which satisfies $\mathbf{r}_{mirror} = -\mathbf{r}_{ghost}$ is considered as shown in Fig. 3. The relation between the mirrored point and the ghost cell must meet the slip wall boundary condition (19), thus yielding

$$\mathbf{q}|_{ghost} = \mathbf{q}|_{mirror}, \tag{23}$$

$$\frac{\partial \mathbf{q}}{\partial n}|_{ghost} = -\frac{\partial \mathbf{q}}{\partial n}|_{mirror}, \tag{24}$$

and using the approximations

$$\frac{\partial \mathbf{q}}{\partial n}|_{mirror} \approx \frac{\mathbf{q}|_{image} - \mathbf{q}|_{mirror}}{\delta - |\mathbf{r}_{mirror}|}, \tag{25}$$

$$\frac{\partial \mathbf{q}}{\partial n}|_{image} \approx \frac{\mathbf{q}|_{extra} - \mathbf{q}|_{image}}{|\mathbf{r}_{extra}|}. \tag{26}$$

Substituting (23), (24) into (22), the necessary relation for the ghost-cell values is derived as

$$\mathbf{q}|_{ghost} = \mathbf{q}|_{image} - \frac{\delta - |\mathbf{r}_{ghost}|}{\delta}(\mathbf{q}|_{extra} - \mathbf{q}|_{image}). \tag{27}$$

Next, to derive the expression for the normal component of the velocity, a quadratic relation approximated between the ghost cell and the projection point can be expressed as

$$u_n|_{ghost} = u_n|_{proj} - |\mathbf{r}_{ghost}| \cdot \frac{\partial u_n}{\partial n}|_{proj} + \frac{|\mathbf{r}_{ghost}|^2}{2} \cdot \frac{\partial^2 u_n}{\partial n^2}|_{proj} \tag{28}$$

In addition, between the extra image point and the image point, a quadratic relation is written as:

$$u_n|_{extra} = u_n|_{image} + |\mathbf{r}_{extra}| \cdot \frac{\partial u_n}{\partial n}|_{image} + \frac{|\mathbf{r}_{extra}|^2}{2} \cdot \frac{\partial^2 u_n}{\partial n^2}|_{image} \tag{29}$$

With a quadratic assumption, the second order derivatives at the projection point and at the image point must be equal, such that

$$\frac{\partial^2 u_n}{\partial n^2}|_{proj} = \frac{\partial^2 u_n}{\partial n^2}|_{image}, \tag{30}$$

and the average slope between the projection point and the image point become equal:

$$\frac{\frac{\partial u_n}{\partial n}|_{proj} + \frac{\partial u_n}{\partial n}|_{image}}{2} = \frac{u_n|_{image} - u_n|_{proj}}{\delta}. \tag{31}$$

For simplicity, the location of the extra image point is defined such that $\mathbf{r}_{extra} = -\mathbf{r}_{ghost}$. Subtracting (29) from (28) and using the relations (30) and (31), the expression for the normal

This article is protected by copyright. All rights reserved.

Accepted Article

component of the velocity at the ghost cell is obtained as

$$\begin{aligned} u_n|_{ghost} &= u_n|_{extra} - u_n|_{image} - |\mathbf{r}_{ghost}| \cdot \frac{2u_n|_{image}}{\delta} \\ &= u_n|_{extra} - (1 + \frac{2|\mathbf{r}_{ghost}|}{\delta})u_n|_{image}. \end{aligned} \tag{32}$$

Using equations (27) and (32), values at the ghost cells are extrapolated from the image points and the extra image points. The values at the image points and the extra image points are obtained using a complete bilinear interpolation.

For compressible flows that may involve discontinuity such as shock waves, higher order extrapolation may result in nonphysical values for the ghost cells. For instance, when a shock wave happens to be positioned between the image point and the extra image point, the extrapolation from these image points may result in negative density or pressure at the ghost cell. To address this issue, a sensor $\alpha$ is introduced for the improved ghost-cell method, defined as the ratio of pressures or densities between the extra image point and the image point as

$$\alpha = \max\left\{ \frac{\max(p|_{image}, p|_{extra})}{\min(p|_{image}, p|_{extra})}, \frac{\max(\rho|_{image}, \rho|_{extra})}{\min(\rho|_{image}, \rho|_{extra})} \right\}. \tag{33}$$

For a chosen threshold $\alpha_0$, the extrapolation for the ghost cells (27) is reduced to the first order when the discontinuity sensor is lager than the threshold while keeping the quadratic extrapolation elsewhere, i.e.

$$\mathbf{q}|_{ghost} = \begin{cases} \mathbf{q}|_{image} - \frac{\delta - |\mathbf{r}_{ghost}|}{\delta}(\mathbf{q}|_{extra} - \mathbf{q}|_{image}) & \text{if } \alpha < \alpha_0 \\ \mathbf{q}|_{image} & \text{if } \alpha \geq \alpha_0. \end{cases} \tag{34}$$

The choice of threshold $\alpha_0$ is problem-dependent. Based on our experience, the recommended values are $1.2 \leq \alpha_0 \leq 2.0$, where solution becomes more stable for lower values and more accurate at higher values.

## 3. TEST SIMULATIONS

In the following, a series of numerical tests are presented in the order of increasing complexities in the configurations, as an attempt to verify the accuracy of the new ghost-cell immersed boundary method in compressible flow problems, in comparison with the baseline ghost-cell method. For selected cases, the computational efficiency of the improved ghost-cell method is compared with that of a cut-cell method.

### *3.1. Double Mach reflection of a strong shock*

A double Mach reflection test, which has often been used as a benchmark for numerical methods for solving Euler equations [30], is a useful tool to check the quality of a numerical scheme because the jet formed along the boundary is known to be highly sensitive to the numerical scheme used. A non-dimensionalized, two-dimensional computational domain of a $2 \times 1$ rectangle is used. An initial planar shock wave of Mach 10 is set at point $x$ = 1/6, $y$ = 0. The pre-shock values of density and pressure are $\rho_0$ = 1.4 and $p_0$ = 1, and the gas constant $\gamma$ = 1.4 is used.

Figure 4(a) shows the ghost-cell immersed boundary case where the boundary for a ramp starting from $x$ = 1/6 with an angle of 30° to the $x$-axis is not aligned with the Cartesian grid, using the baseline method discussed in Section 2.4.3. The shock wave travels to the right in a direction normal to $x$. Figure 4b shows the equivalent grid-aligned case set up by rotational transformation, where the shock wave moves with an angle of 30° to the $x$-axis and the domain boundary at the bottom is reflective from $x$ = 1/6. This configuration does not require a ghost-cell method, and will be used as a reference for comparison. The moving shocks relative to the solid boundaries are identical in both cases. In Fig. 4c the density contours of the ghost-cell method case (red) are overlapped

This article is protected by copyright. All rights reserved.

Accepted Article

with the grid aligned case (grey) by a rotation of 30°, demonstrating that the slip-wall boundary condition implicitly represented by the ghost-cell method is consistently implemented. Despite this overall agreement between ghost-cell case and grid-aligned case, it is notable that the jet developed along the ramp wall, right behind the leading Mach stem, is more diffused with the baseline ghost-cell boundary method (Fig. 4(a) than with the grid-aligned case (Fig. 4b). This difference is more pronounced with a refined grid to be shown in the following.

Figure 5 shows the results for the same problem with a finer resolution, 800 $\times$200, for which detailed flow structures near the Mach stems are well resolved. While the structure of the jet along the wall is captured well in the grid-aligned case (Fig. 5(b)), the jet along the ramp wall with the baseline ghost-cell method (Fig. 5(a)) is more diffusive, hence the detachment of the jet front and the leading Mach stem is not clearly captured. This discrepancy may be attributed to the incomplete bilinear interpolation of the baseline ghost-cell boundary method. The poor resolution of the flow structure around the leading Mach stem with the baseline ghost-cell boundary method is demonstrated to be improved with the proposed ghost-cell method introduced in Section 2.4.4 as shown in the following.

Figure 6 shows the results of the improved ghost-cell boundary method at resolutions of 400 $\times$ 200 and 800 $\times$ 400, respectively. Compared to the baseline ghost-cell method, the jet structure in the double Mach region for the improved ghost-cell method is in better agreement to the corresponding grid-aligned case. In particular, in both cases, the leading edge of the jet intersects the boundary at a right angle, which is considered a physically correct result. The density along the ramp wall is shown in Fig. 7 for the grid-aligned case as a reference, and for both baseline and improved ghost-cell boundary methods. The density obtained with the improved ghost-cell boundary method is in suprisingly good agreement with that obtained in the grid-aligned case, showing the identical location of leading Mach stem. With the baseline ghost-cell method, the jet flow was observed to be approaching the leading Mach stem without being resolved distinguishably as pointed out above. This poor resolution of the baseline method resulted in the mismatch of the Mach stem location in this figure. The second peak of the density due to the jet flow, between the distance of 1 and 1.1, was captured with both the improved ghost-cell boundary method and the grid-aligned case, whereas it was merged to the leading density jump with the baseline ghost-cell boundary method, which accounts for the discrepancy in the location of Mach stem with respect to the other two.

With the same test case, solutions with a cut-cell method were also obtained using the Chombo package [22, 23], as shown in Fig. 8. Although the present study is about improving the ghost-cell boundary method, the solutions with the cut-cell method is included for this test case to show how the improved ghost-cell boundary method performs in comparison with the cut-cell method. In cut-cell method readily available in EBAMRGodunov solver of Chombo package, an equivalent PPM reconstruction employed the van Leer limiter for characteristic variables for the fourth order slope calculation and for the primitive variable Riemann solver. As such, the comparison between the two methods should be considered fair as both approaches employed the equivalent second order finite volume method. In the result with the cut-cell method, the Mach stem and jet structure developed along the ramp wall is resolved accurately. Comparing Fig. 5(a), Fig. 6b, and Fig. 8(b) at a same resolution of 800 $\times$ 400, it is verified that the improved ghost-cell immersed boundary method resolves the solution along the immersed boundary as accurately as the cut-cell method.

Finally, a direct comparison between the improved ghost-cell method and the cut-cell method is presented with the AMR capability activated. Figs. 9 and 10 are the results obtained from the cut-cell and the improved ghost-cell methods, respectively. In Fig. 9b, mesh in the boundary grids are not refined, and refinements only take place around the discontinuities in fluid domain. This is because geometry resolution is independent of mesh resolution in this case, thus there is no need to refine the boundary grids. Through the comparison, it is also found that the relative distance from the jet front to the front mach stem is farther in Fig. 10, and the relative distance in Fig. 9 is closer to the results in [30]. Considering that in this particular test the solution of jet formation along the wall is known to be sensitive to the numerical method applied, the solution with the improved ghost-cell method is in good agreement with the cut-cell method.

This article is protected by copyright. All rights reserved.

In summary, with this test of double Mach reflection over a ramp, the failure of the solution with the baseline ghost-cell method and the cure of it with the improved ghost-cell method was demonstrated clearly. The capability of capturing jet front along the wall with respect to the leading Mach stem using the improved ghost-cell method was proven by the comparison with both the grid-aligned case and the cut-cell method.

### *3.2. A Mach 3 wind tunnel with a forward facing step*

The classical Woodward-Colella test for a forward facing step [30] is chosen next in order to validate the accuracy of the improved ghost-cell immersed boundary method for grid-aligned geometries. The computational domain is a $3 \times 1$ rectangle, where the leading edge of a forward-facing step of height 0.2 is located at $x = 0.6$. The initial flow field is defined with a density $\rho = 1.4$, a pressure $p = 1.0$ and a horizontal velocity of Mach = 3, with $\gamma = 1.4$ for an ideal gas. The top boundary of the channel is set to be a slip wall.

Figure 11 shows the results with the boundary treatment using the baseline and the improved ghost-cell method, respectively. In the test, overexpansion flow strikes the upper surface of the step, causing a weak oblique shock. Both methods yield well-resolved contact discontinuity. In this case with the grid aligned to the boundary, the incomplete bilinear interpolation is not occurring with the baseline ghost-cell method. As we can see, the improved ghost-cell method does not lose its generality dealing with grid-alined boundary, and sharp corner of the boundary.

### *3.3. Supersonic flow over a circular cylinder*

The next step is to verify the improved ghost-cell method in dealing with a curved boundary. A square computational domain of 4 cm $\times$ 4 cm contains a circular cylinder with a radius $r = 0.5$ cm at the center. Initially, a uniform supersonic flow is set in the entire domain at pressure $p_0 = 10^5$ Pa and Mach number $M_0 = 3$. A CFL number of 0.5 is used in the computation.

Figure 12 shows the comparison of density and pressure isocontours when the supersonic flow pasts the circular cylinder, where a zoomed-in partial domain of $x = [1{:}2]$ and $y = [1{:}3]$ is shown for clear illustration. With both methods, the bow shock waves detached from the cylinder is well resolved with smooth isocontours in the post-shock area along the curved geometry.

For a quantitative accuracy assessment, the pressure coefficient along the cylinder surface is calculated:

$$C_p = \frac{\frac{p}{p_0} - 1}{\frac{1}{2}\gamma M_0^2}. \tag{35}$$

Figure 13 shows the pressure coefficient along the cylinder surface as function of the $x$-coordinate, comparing the baseline ghost-cell method and the improved ghost-cell method with the body-fitted grid case from [31]. A uniform Cartesian grid with a resolution of $350 \times 350$ was used in order to approximately match the number of grids placed along the solid boundary with the body-fitted grid. The pressure coefficient based on the improved ghost-cell methods is more approaching to the body-fitted grid case compared to the baseline ghost-cell method, indicating a better accuracy resolving the curved solid boundary.

### *3.4. Prandtl-Meyer expansion*

Steady state calculation of the Prandtl-Meyer expansion waves are often chosen to evaluate the accuracy of the immersed boundary quantitatively [7, 32] by a direct comparison with the exact solutions, which is a smooth flow with constant entropy $S = p/\rho^\gamma$. Therefore, the next test problem considers a Mach 1.3 flow turning over an angle of 20°. The geometry used for a smooth expansion, adjusted from [3], is described as

$$y = \begin{cases} 0.3 & x \le 0.1, \\ 0.3(1 - (x - 0.1)^2) & 0.1 \le x \le 0.7, \\ 0.192 - 0.36(x - 0.7) & x \ge 0.7. \end{cases} \tag{36}$$

This article is protected by copyright. All rights reserved.

Figure 14 shows the density isocontour plot for a uniform 200 $\times$ 200 grid when the flow reaches a steady state. For a range of grid resolutions from 50 $\times$ 50 to 400 $\times$ 400, the errors for the entropy values in the fluid domain are tabulated in Table I. With the errors related to $Ch^p$, where $h$ is the cell size and $C$ is a constant, the order of accuracy $p$ can be obtained numerically.

Table **??** suggests that the $L^\infty$ norm error converges at a higher rate with the improved ghost-cell method than with the baseline ghost-cell method. Moreover, the improved ghost-cell method produces smaller absolute errors for the same grid resolutions. Therefore, it is demonstrated quantitatively that the improved ghost-cell method has better accuracy compared to the baseline ghost-cell method. Overall, the improved ghost-cell method can reach formally second order in $L^1$ and higher order in $L^\infty$ errors. From the convergence study in [9], it is known that the cut-cell method in Chombo is second-order accurate in $L^1$, and first-order accurate in $L^\infty$, which is comparable to the accuracy of the improved ghost-cell method.

### *3.5. CPU time comparison*

To compare the efficiency of the improved ghost-cell method and the cut-cell method, CPU time has been measured through simulations with a single core of CPU for the double Mach reflection case and the circular cylinder supersonic flow case. For these tests, AMR has not been activated in order to eliminate other factors such as the difference in the level of refinement that might affect the computational costs. Table II shows the comparison of the CPU times by each methods, respectively, for the two test cases discussed in previous sections.

It is found that the computational cost using the improved ghost-cell method is approximately half of that with the cut-cell method for the test cases. Therefore, it is concluded that the improved ghost-cell method achieves the same level of accuracy as the cut-cell method, at a significantly improved computational efficiency and simplicity.

## 4. CONCLUSIONS

In this paper, an improved ghost-cell method coupled with a level-set technique for boundary treatment was proposed and implemented in compressible flow simulations. To deal with the too-close ghost-cell issue, the method employed complete bilinear interpolation and higher-order extrapolation schemes. The new method was found to reach a second-order accuracy in $L^1$ norm and higher than first order in $L^\infty$ norm. Compared to the baseline ghost-cell method, the improved ghost-cell method is verified to be more accurate for boundary treatment. The comparison between the improved ghost-cell method and the cut-cell method also demonstrated that the two methods have comparable accuracy in capturing flows around solid boundaries, while the improved ghost-cell method was found to be more efficient than the cut-cell method, easy to implement without the need to modify the underlying numerical methods. As demonstrated in detailed mathematical descriptions, the new method can be readily implemented for the constructions of too-close ghost-cell values for both Neumann and Dirichlet boundary conditions, suggesting that the extension of the method to simulations of Navier-Stokes equations is straightforward.

ACKNOWLEDGEMENT

The work reported in this study was supported by the King Abdullah University of Science and Technology (KAUST).

## REFERENCES

[1] D. K. Clarke, H. A. Hassan, and M. D. Salas, *Euler calculations for multielement airfoils using Cartesian grids*, AIAA Journal **24** (19862015/05/27), no. 3, 353–358.

[2] I-Liang Chern and Phillip Colella, *A conservative front tracking method for hyperbolic conservation laws*, Technical Report UCRL-97200, Lawrence Livermore National Laboratory, 1987.

This article is protected by copyright. All rights reserved.

Accepted Article

[3] M. J. Berger and R. J. LeVeque, *Stable boundary conditions for Cartesian grid calculations*, Computing Systems in Engineering **1** (1990), no. 2–4, 305–311.

[4] X. Y. Hu, B. C. Khoo, N. A. Adams, and F. L. Huang, *A conservative interface method for compressible flows*, Journal of Computational Physics **219** (2006), no. 2, 553–578. MR2274949

[5] James J. Quirk, *An alternative to unstructured grids for computing gas dynamic flows around arbitrarily complex two-dimensional bodies*, Computers & Fluids **23** (19941), no. 1, 125–142.

[6] John B. Bell, Phillip Colella, and Michael L. Welcome, *Conservative front-tracking for inviscid compressible flow*, Aiaa 10th computational fluid dynamics conference, 1991.

[7] Richard B. Pember, John B. Bell, Phillip Colella, William Y. Crutchfield, and Michael L. Welcome, *An adaptive Cartesian grid method for unsteady compressible flow in irregular regions*, Journal of Computational Physics **120** (1995), no. 2, 278–304. MR1349463 (96d:76081)

[8] D. Modiano and P. Colella, *A higher-order embedded boundary method for time-dependent simulation of hyperbolic conservation laws*, Technical Report LBNL-45239, Lawrence Livermore National Laboratory, 2000.

[9] Phillip Colella, Daniel T. Graves, Benjamin J. Keen, and David Modiano, *A Cartesian grid embedded boundary method for hyperbolic conservation laws*, Journal of Computational Physics **211** (2006), no. 1, 347–366. MR2168881 (2006i:65142)

[10] Daniel T. Graves, Phillip Colella, David Modiano, Jeffrey Johnson, Bjorn Sjogreen, and Xinfeng Gao, *A Cartesian grid embedded boundary method for the compressible Navier-Stokes equations*, Communications in Applied Mathematics and Computational Science **8** (2013), no. 1, 99–122. MR3143820

[11] Ronald P. Fedkiw, Tariq Aslam, Barry Merriman, and Stanley Osher, *A non-oscillatory Eulerian approach to interfaces in multimaterial flows (the ghost fluid method)*, Journal of Computational Physics **152** (1999), no. 2, 457–492. MR1699710 (2000c:76061)

[12] Stanley Osher and Ronald Fedkiw, *Level set methods and dynamic implicit surfaces*, Springer-Verlag, New York, 2003. MR1939127 (2003j:65002)

[13] Marco Arienti, Patrick Hung, Eric Morano, and Joseph E. Shepherd, *A level set approach to Eulerian–Lagrangian coupling*, Journal of Computational Physics **185** (20032), no. 1, 213–251.

[14] T. Ménard, S. Tanguy, and A. Berlemont, *Coupling level set/VOF/ghost fluid methods: Validation and application to 3D simulation of the primary break-up of a liquid jet*, International Journal of Multiphase Flow **33** (20075), no. 5, 510–524.

[15] Paul Macklin and John S. Lowengrub, *A new ghost cell/level set method for moving boundary problems: application to tumor growth*, Journal of Scientific Computing **35** (2008), no. 2-3, 266–299. MR2429941 (2009h:65119)

[16] Yannick Gorsse, Angelo Iollo, Haysam Telib, and Lisl Weynans, *A simple second order Cartesian scheme for compressible Euler flows*, Journal of Computational Physics **231** (2012), no. 23, 7780–7794. MR2972868

[17] Kazuhiro Nakahashi, *Immersed boundary method for compressible Euler equations in the building-cube method*, 20th aiaa computational fluid dynamics conference, 20112015/05/27.

[18] Ralf Deiterding, Raul Radovitzky, Sean P. Mauch, Ludovic Noels, Julian C. Cummings, and Daniel I. Meiron, *A virtual test facility for the efficient simulation of solid material response under strong shock and detonation wave loading*, Engineering with Computers **22** (2006), no. 3-4, 325–347.

[19] Rajat Mittal and Gianluca Iaccarino, *Immersed boundary methods*, Annual Review of Fluid Mechanics **37** (2005), 239–261. MR2115343 (2005m:76137)

[20] R. Ghias, R. Mittal, and H. Dong, *A sharp interface immersed boundary method for compressible viscous flows*, Journal of Computational Physics **225** (2007), no. 1, 528–553. MR2346690 (2008g:76094)

[21] Dartzi Pan and Tzung-Tza Shen, *Computation of incompressible flows with immersed bodies by a simple ghost cell method*, International Journal for Numerical Methods in Fluids **60** (2009), no. 12, 1378–1401. MR2554919 (2010i:65161)

[22] M. Adams, P. Colella, D. T. Graves, J. N. Johnson, H. S. Johansen, N. D. Keen, T. J. Ligocki, D. F. Martin, P. W. McCorquodale, D. Modiano, P. O. Schwartz, T. D. Sternberg, and B. Van Straalen, *Chombo software package for AMR applications design document*, Technical Report LBNL-6616E, Lawrence Berkeley National Laboratory, 2014.

[23] P. Colella, D. T. Graves, T. J. Ligocki, G. H. Miller, P. O. Schwartz D. Modiano, B. Van Straalen, J. Pillod, D. Trebotich, and M. Barad, *EBChombo software package for Cartesian grid, embedded boundary applications*, Technical Report LBNL-6615E, Lawrence Berkeley National Laboratory, 2014.

[24] Phillip Colella and Paul R Woodward, *The piecewise parabolic method (PPM) for gas-dynamical simulations*, Journal of Computational Physics **54** (19844), no. 1, 174–201.

This article is protected by copyright. All rights reserved.

Accepted Article

[25] Eleuterio F. Toro, *Riemann solvers and numerical methods for fluid dynamics*, Third, Springer-Verlag, Berlin, 2009. MR2731357 (2011i:76059)

[26] *BoxLib*, 2014.

[27] Stanley Osher and James A. Sethian, *Fronts propagating with curvature-dependent speed: algorithms based on Hamilton-Jacobi formulations*, Journal of Computational Physics **79** (1988), no. 1, 12–49. MR965860 (89h:80012)

[28] J. A. Sethian, *Level set methods and fast marching methods*, Cambridge Monographs on Applied and Computational Mathematics, Cambridge University Press, Cambridge, 1999. MR1700751 (2000c:65015)

[29] ———, *Evolution, implementation, and application of level set and fast marching methods for advancing fronts*, Journal of Computational Physics **169** (2001), no. 2, 503–555. MR1836524 (2002c:76074)

[30] Paul Woodward and Phillip Colella, *The numerical simulation of two-dimensional fluid flow with strong shocks*, Journal of Computational Physics **54** (1984), no. 1, 115–173. MR748569 (85e:76004)

[31] Björn Sjögreen and N. Anders Petersson, *A Cartesian embedded boundary method for hyperbolic conservation laws*, Communications in Computational Physics **2** (2007), no. 6, 1199–1219. MR2359084 (2008j:65135)

[32] Hans Forrer and Rolf Jeltsch, *A higher-order boundary treatment for Cartesian-grid methods*, Journal of Computational Physics **140** (1998), no. 2, 259–277. MR1616130 (98m:76107)

Accepted Article

This article is protected by copyright. All rights reserved.

Accepted Article

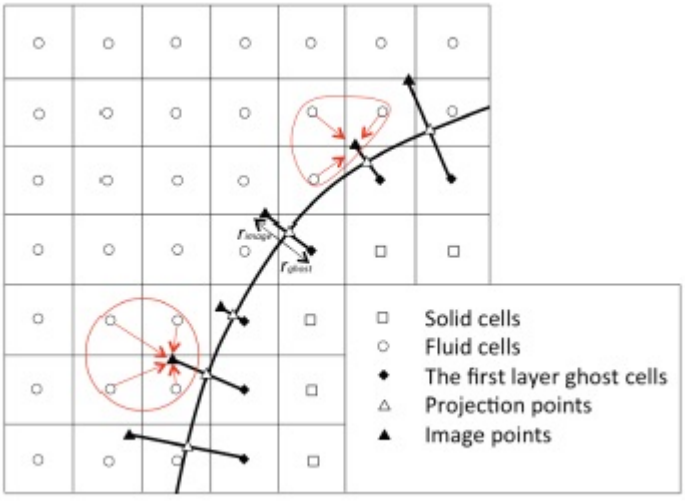


Figure 1. Relative positions of ghost cells, projection points, image points and the surrounding fluid cells for a bilinear interpolation.

This article is protected by copyright. All rights reserved.

Accepted Article

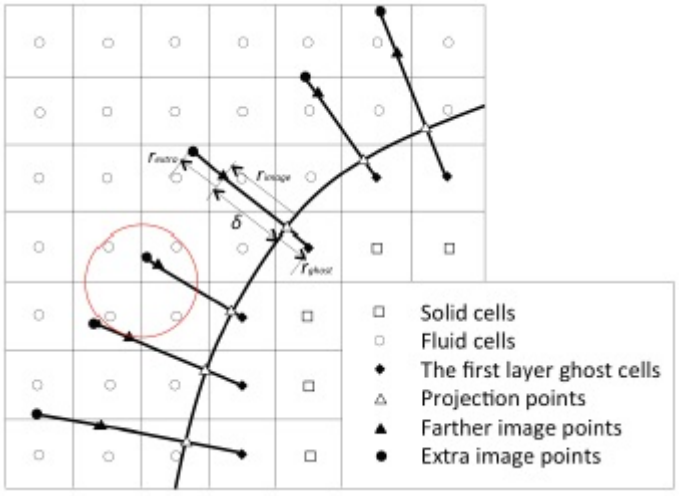


Figure 2. Relative positions of ghost cells, projection points, farther image points and extra image points, $\delta = \sqrt{2}\Delta x$ is the constant distance from the projection point to the image point.

This article is protected by copyright. All rights reserved.

Accepted Article

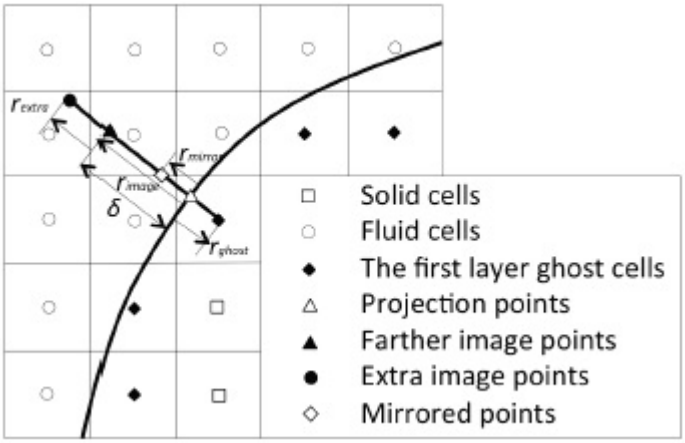


Figure 3. Relative positions of ghost cells, projection points, mirrored points, farther image points and extra image points.

This article is protected by copyright. All rights reserved.

Accepted Article

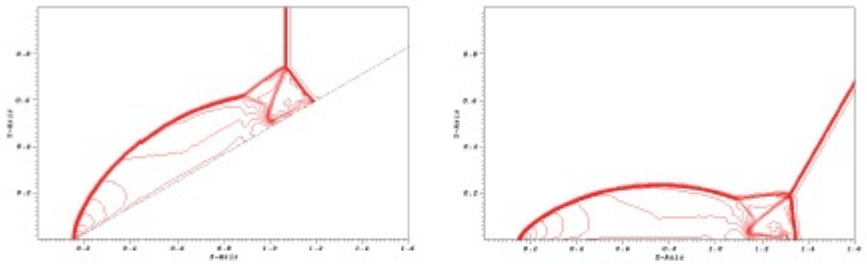

(a) Ghost-cell ramp case

(b) Grid-aligned case

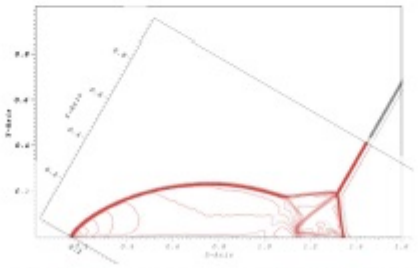

(c) Overlap contours in red are from (a) and in grey are from (b)

Figure 4. Baseline ghost-cell boundary calculation of DMR: 30 contours of density from 1.4 to 23. Fixed grid 400 $\times$ 200, CFL=0.8, t=0.09.

This article is protected by copyright. All rights reserved.

Accepted Article

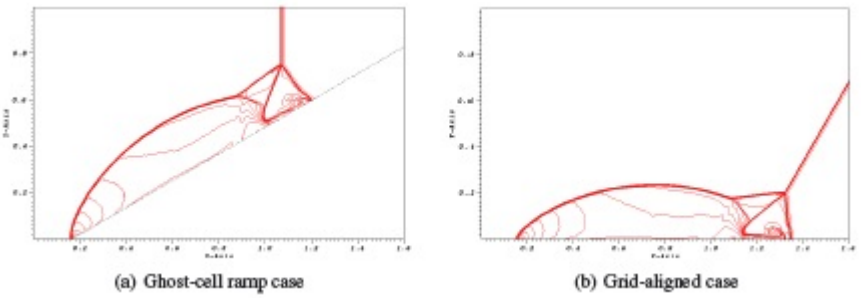

(a) Ghost-cell ramp case (b) Grid-aligned case

Figure 5. Baseline ghost-cell boundary calculation of DMR: 30 contours of density from 1.4 to 23. Fixed grid $800 \times 400$, CFL=0.8, t=0.09.

This article is protected by copyright. All rights reserved.

Accepted Article

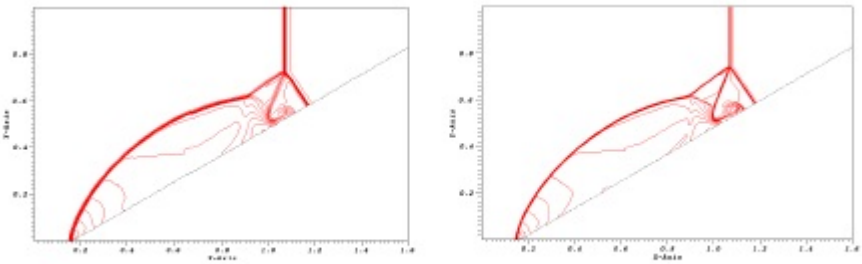


Figure 6. Improved ghost-cell boundary calculation of DMR: 30 contours of density from 1.4 to 23, CFL=0.8, t=0.09.

This article is protected by copyright. All rights reserved.

Accepted Article



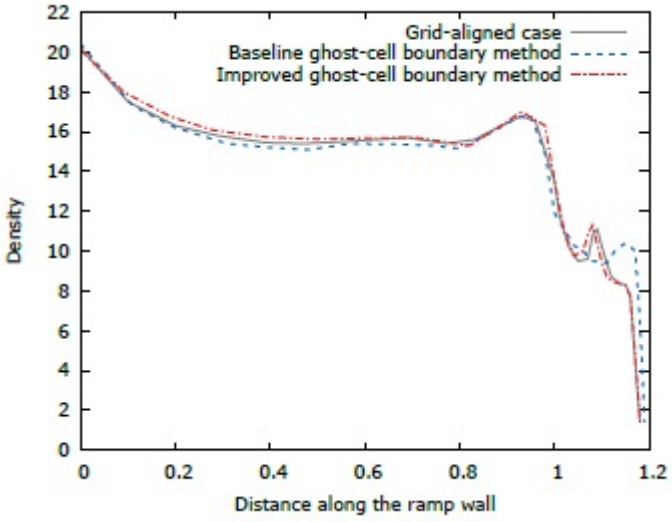


Figure 7. Density along the ramp wall, 800 $\times$ 400 fixed grid.

This article is protected by copyright. All rights reserved.

Accepted Article

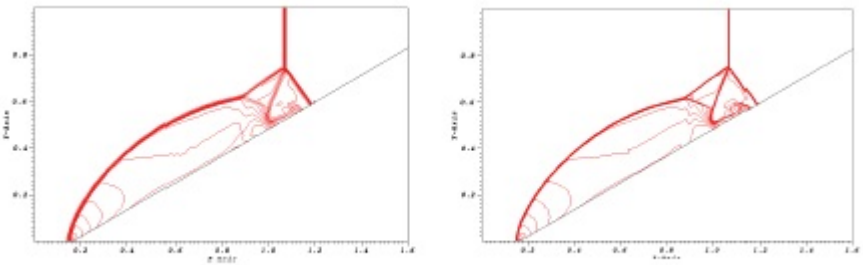

(a) 400 × 200 (b) 800 × 400

Figure 8. Cut-cell boundary (Chombo) calculation of DMR: 30 contours of density from 1.4 to 23, CFL=0.8, t=0.09.

This article is protected by copyright. All rights reserved.

Accepted Article

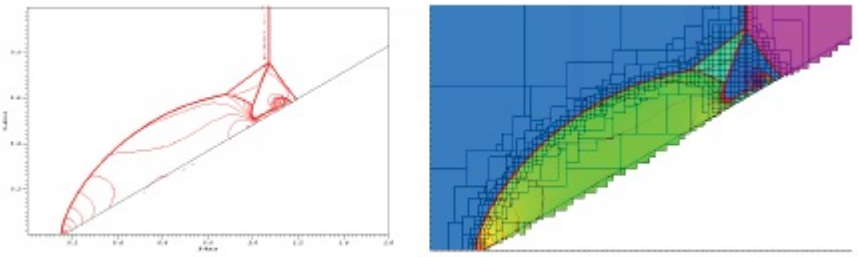

(a) 30 density contours from 1.4 to 23. (b) density plot with AMR grid hierarchy.

Figure 9. Cut-cell boundary (Chombo) calculation of DMR. The effective grid resolution at the finest level is $1600 \times 800$, CFL=0.8, t=0.09.

This article is protected by copyright. All rights reserved.

Accepted Article

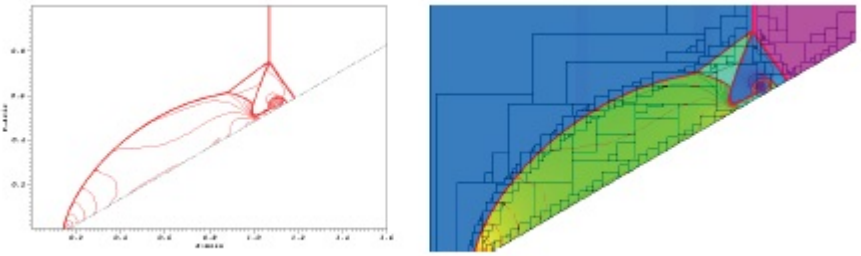

(a) 30 density contours from 1.4 to 23. (b) density plot with AMR grid hierarchy.

Figure 10. Improved ghost-cell boundary calculation of DMR. The effective grid resolution at the finest level is $1600 \times 800$, CFL=0.8, t=0.09.

This article is protected by copyright. All rights reserved.

Accepted Article



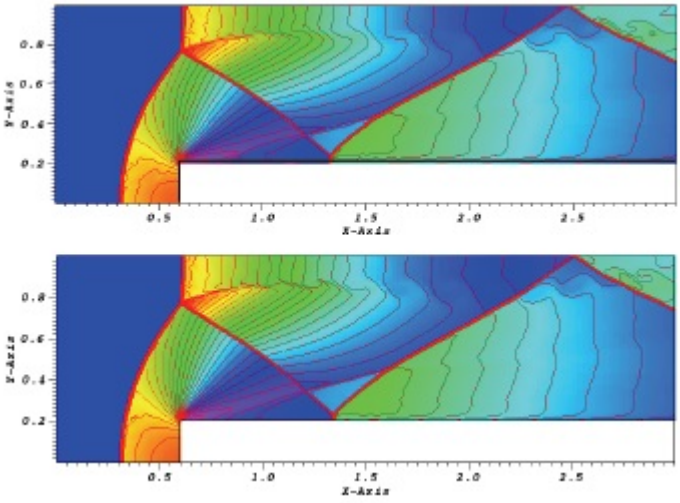


Figure 11. Baseline (top) and improved (bottom) ghost-cell boundary calculation of forward facing step problem: the density field with 30 equal interval isocontours from 0 to 6.5; The effective grid resolution at finest level is 480 $\times$ 160, CFL=0.8, t=4.0.

This article is protected by copyright. All rights reserved.

Accepted Article

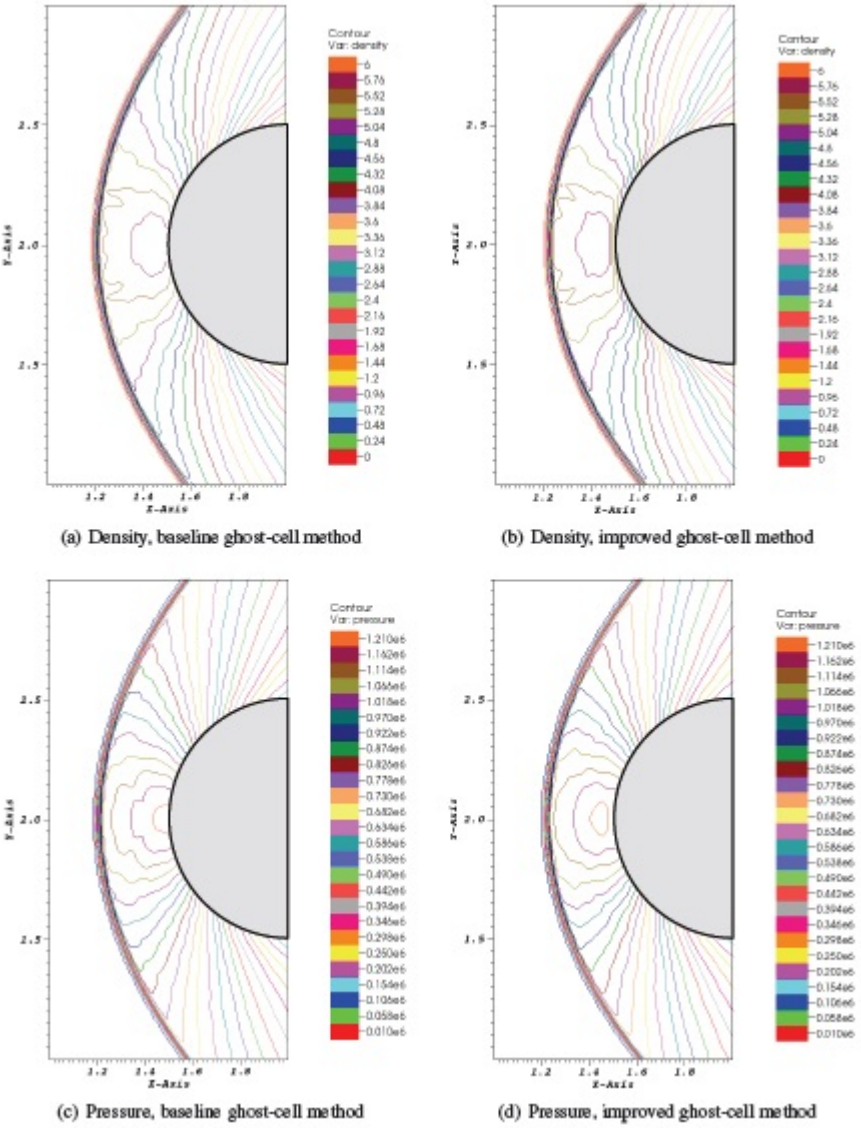


Figure 12. Comparison between the baseline ghost-cell method and the improved ghost-cell method for a Mach 3 supersonic flow over a circular cylinder. Fixed grid 350 $\times$ 350, CFL=0.5, t=1.5.

This article is protected by copyright. All rights reserved.

Accepted Article

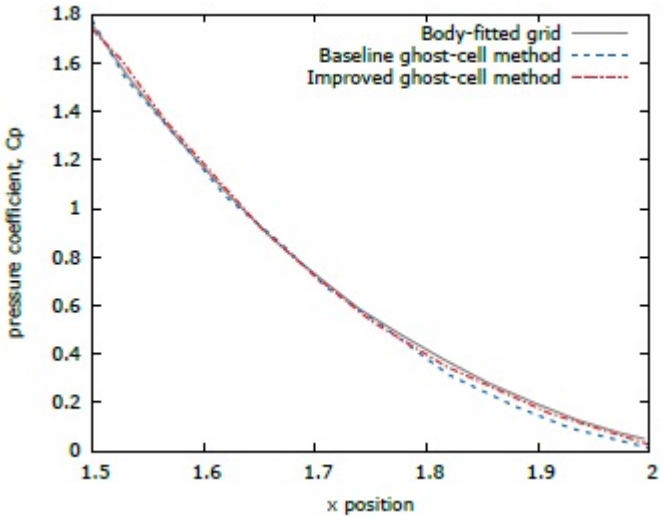


Figure 13. Comparison of pressure coefficients for a Mach 3 supersonic flow over a circular cylinder obtained from the improved ghost-cell method, the cut-cell method and the result for body-fitted grid from [31].

This article is protected by copyright. All rights reserved.

Accepted Article

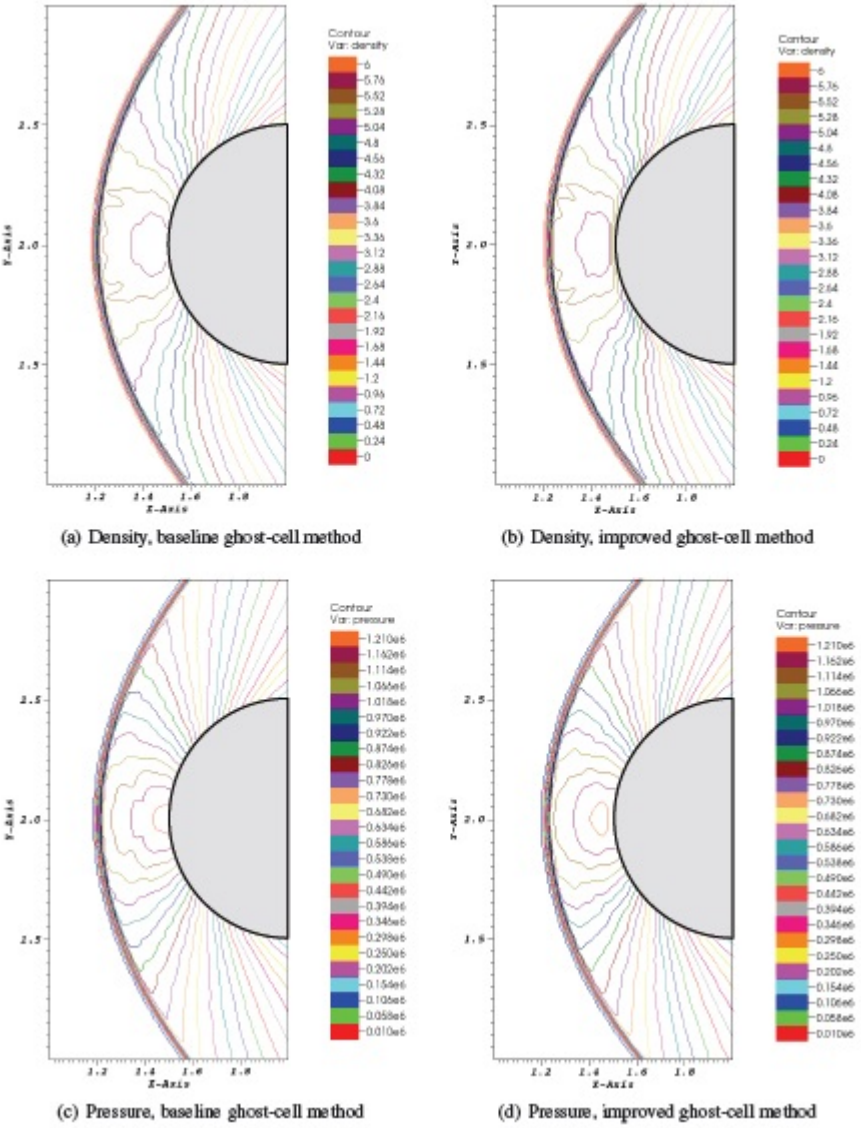


(a) Density, baseline ghost-cell method

(b) Density, improved ghost-cell method

(c) Pressure, baseline ghost-cell method

(d) Pressure, improved ghost-cell method

Figure 14. Density isocontours for Prandtl-Meyer expansion wave resulting from a Mach 1.3 flow turning over an angle of 20°.

This article is protected by copyright. All rights reserved.

Accepted Article

Table I. Convergence rate of entropy

| Method | grid(h) | $L^1$ | order | $L^2$ | order | $L^\infty$ | order |
|---|---|---|---|---|---|---|---|
| baseline ghost-cell method | $50 \times 50$ | 1.06e-05 | - | 4.32e-05 | - | 4.74e-04 | - |
| | $100 \times 100$ | 3.11e-06 | 1.77 | 1.42e-05 | 1.61 | 2.49e-04 | 0.93 |
| | $200 \times 200$ | 9.73e-07 | 1.68 | 5.45e-06 | 1.38 | 1.49e-04 | 0.74 |
| | $400 \times 400$ | 2.51e-07 | 1.95 | 1.60e-06 | 1.77 | 7.63e-05 | 0.97 |
| improved ghost-cell method | $50 \times 50$ | 6.44e-06 | - | 2.47e-05 | - | 1.58e-04 | - |
| | $100 \times 100$ | 1.82e-06 | 1.82 | 9.00e-06 | 1.46 | 7.99e-05 | 0.98 |
| | $200 \times 200$ | 4.60e-07 | 1.98 | 2.89e-06 | 1.64 | 3.39e-05 | 1.24 |
| | $400 \times 400$ | 1.19e-07 | 1.95 | 9.41e-06 | 1.62 | 1.47e-05 | 1.21 |

This article is protected by copyright. All rights reserved.

Accepted Article

Table II. CPU time comparison

| CPU time (s) | improved ghost-cell Method | cut-cell method |
|---|---|---|
| Double Mach reflection case | 185 | 303 |
| Circular cylinder supersonic flow case | 894 | 1880 |

This article is protected by copyright. All rights reserved.